Inverse-kinematics proton scattering from ^{42,44}S, ^{41,43}P, and the collapse of the $N = 28$ major shell closure

L. A. Riley,[1] D. Bazin,[2,3] J. Belarge,[2,3,*] P. C. Bender,[2] B. A. Brown,[2,3] P. D. Cottle,[4] B. Elman,[2,3] A. Gade,[2,3] S. D. Gregory,[1] E. B. Haldeman,[1] K. W. Kemper,[4] B. R. Klybor,[1] M. A. Liggett,[1] S. Lipschutz,[2,3] B. Longfellow,[2,3] E. Lunderberg,[2,3] T. Mijatovic,[2] J. Pereira,[2,3] L. M. Skiles,[1] R. Titus,[2,3] A. Volya,[4] D. Weisshaar,[2] J. C. Zamora,[2] and R. G. T. Zegers[2,3,5]

[1]*Department of Physics and Astronomy, Ursinus College, Collegeville, Pennsylvania 19426, USA*
[2]*National Superconducting Cyclotron Laboratory, Michigan State University, East Lansing, Michigan 48824, USA*
[3]*Department of Physics and Astronomy, Michigan State University, East Lansing, Michigan 48824, USA*
[4]*Department of Physics, Florida State University, Tallahassee, Florida 32306, USA*
[5]*Joint Institute for Nuclear Astrophysics-Center for the Evolution of the Elements, Michigan State University, East Lansing, Michigan 48824, USA*

(Received 30 March 2019; revised manuscript received 17 July 2019; published 17 October 2019)

Excited states of the neutron-rich isotopes ^{42,44}S and ^{41,43}P have been studied via inverse-kinematics proton scattering from a liquid hydrogen target, using the GRETINA γ-ray tracking array to extract inelastic-scattering cross sections. Deformation lengths of the 2_1^+ excitations in ^{42,44}S have been determined and, when combined with deformation lengths determined with electromagnetic probes, yield the ratio of neutron-to-proton matrix elements M_n/M_p for the 2_1^+ excitations in these nuclei. The present results for ^{41,43}P(p, p') are used to compare two shell-model interactions, SDPF-U and SDPF-MU. As in a recent study of ^{42}Si, the present results on ^{41,43}P favor the SDPF-MU interaction.

DOI: 10.1103/PhysRevC.100.044312

I. INTRODUCTION

One of the highest scientific priorities for nuclear structure physicists during the last few decades has been to determine the behavior of the major neutron shell closure at $N = 28$ and to understand the mechanism underlying its collapse in neutron-rich nuclei near ^{42}Si, which is close to the neutron drip line. This shell closure is strongly defined in the stable $N = 28$ isotone ^{48}Ca, but appears to narrow and then collapse as protons are removed. The energy of the 2_1^+ state decreases from 3832 keV in ^{48}Ca [1] to 1329 keV in the radioactive nucleus ^{44}S [2,3] and then to 742 keV in ^{42}Si [4]. In fact, the 2_1^+ state energy in ^{42}Si is lower than it is in the $N = 26$ isotope ^{40}Si (986 keV [5]) so that the most recognizable signature of a major shell closure—a significant increase in the energy of the 2_1^+ state—has disappeared entirely in the Si isotopes at $N = 28$.

In the present work, we report results of inelastic proton-scattering studies of the radioactive $N = 28$ isotones ^{44}S and ^{43}P and the $N = 26$ isotones ^{42}S and ^{41}P performed in inverse kinematics with a liquid hydrogen target to uncover several new aspects of the behavior of nuclei in the vicinity of ^{42}Si. In ^{42,44}S, we are able to compare the results of the present inelastic-scattering measurement of the 2_1^+ states to previous Coulomb excitation measurements of the same transitions to determine whether the excitations of these states are isoscalar. In addition, we use the results of the ^{41,43}P(p, p') measurements to compare the SDPF-U and SDPF-MU shell-model interactions, as was done in a recent study of ^{42}Si [6].

II. EXPERIMENTAL DETAILS

The experiment was performed at the Coupled-Cyclotron Facility of the National Superconducting Cyclotron Laboratory at Michigan State University (NSCL) [7]. The secondary beams were produced by fragmentation of a 140 MeV/nucleon ^{48}Ca primary beam in a 1222 mg/cm^2 ^{9}Be production target and separated by the A1900 fragment separator [8]. The momentum acceptance of the A1900 was set to 2%. A 300 mg/cm^2 aluminum achromatic wedge was used to further separate the secondary beams by Z. The beams of interest in the present work were produced with two magnet settings of the A1900 and are summarized in Table I.

Secondary beam particles were identified upstream of the reaction target by times of flight from the A1900 extended focal plane and the object position of the S800 spectrograph [9]. A scintillator in the focal plane of the S800 was used to stop both timing measurements. The beam then passed through the NSCL/Ursinus College liquid hydrogen target, based on the design of Ryuto *et al.* [10]. The target was installed at the target position of the S800. Outgoing beam particles were identified by energy loss in the S800 ionization chamber and time of flight. The reaction kinematics were such that all

*J. Belarge is currently a MIT Lincoln Laboratory employee. No Laboratory funding or resources were used to produce the results/findings reported in this article.

TABLE I. Secondary beam properties and yields.

Secondary Beam	Purity (%)	Midtarget energy (MeV/nucleon)	MidTarget v/c	Total particles
^{42}S	2	62.5	0.349	9.46×10^5
^{41}P	30	57.7	0.336	1.37×10^7
^{44}S	32	70.2	0.368	5.14×10^6
^{43}P	9	64.7	0.354	1.37×10^6

four beams, over the full range of possible projectile kinetic energies within the target, were scattered into laboratory angles below 2°, falling entirely within the 7° × 10° angular acceptance of the S800. The GRETINA γ-ray tracking array [11,12] was centered on the target. Eight modules housing four 36-fold segmented high-purity germanium crystals were installed on one of the GRETINA mounting hemispheres to accommodate the target. Two modules were centered at 58°, four at 90°, and two at 122° with respect to the beam axis.

The liquid hydrogen was contained by a cylindrical aluminum target cell, with a 125-μm Kapton entrance and exit windows, mounted on a cryocooler. The nominal target thickness was 30 mm. The target cell and the cryocooler were surrounded by a 1-mm-thick aluminum radiation shield with entrance and exit windows covered by 5-μm aluminized Mylar foil. The temperature and the pressure of the target cell at 17.00(25) K and 880(10) Torr were monitored throughout the experiment. The variations in the temperature and the pressure of the target cell corresponded to a 0.3% uncertainty in target density.

The pressure difference across the Kapton entrance and exit windows caused them to bulge outward. The resulting additional target thickness was determined by fitting GEANT4 [13] simulations of the beam particles traversing the target to the measured kinetic energy distribution of the outgoing beam particles. Before the liquid hydrogen target was filled, the kinetic energy spectra of the secondary beams passing through the empty target cell were measured. Simulations of the beams passing through the full target were run in which initial beam energies were drawn from these measured empty-cell kinetic energy distributions. The thickness of the outward bulge of the Kapton entrance and exit windows was varied in the simulations of each beam, and the resulting outgoing kinetic energy distributions were fit by a simple scaling of the simulated spectra.

Measured kinetic energy spectra of the beams after traversing the full target, relative to the kinetic energy corresponding to the center of the S800 momentum acceptance, are shown in Fig. 1. The dashed spectra in the four main panels of Fig. 1 are simulated spectra assuming the target bulge thickness giving the best fit to the measured spectra. The insets show the figure of merit from the log-likelihood fitting procedure

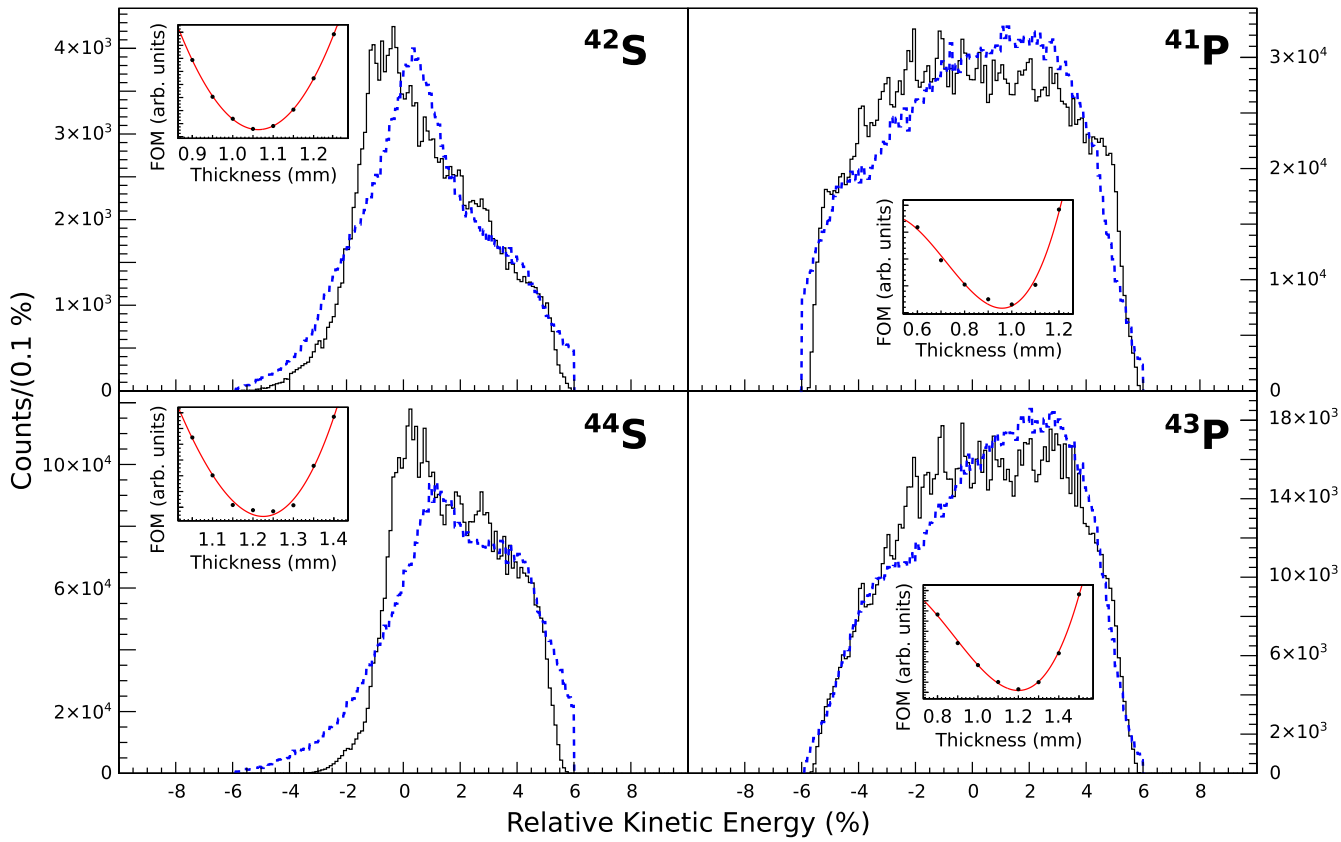

FIG. 1. Relative kinetic energy spectra of the beams measured downstream of the target in the S800. The dashed spectra are the GEANT4 fits described in the text. The insets are plots of the figure of merit from log-likelihood fits of the simulated beam particles vs the thickness of the outward bulge of the Kapton entrance and exit windows of the target.

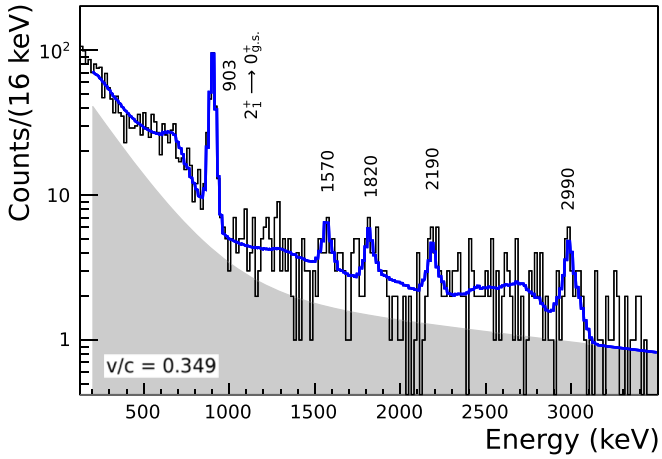

FIG. 2. Projectile-frame spectrum of ^{42}S measured via inverse-kinematics proton scattering.

plotted vs the simulated window bulge thickness. This process yielded best-fit bulge thicknesses of 1.06 and 0.96 mm for the ^{42}S and ^{41}P beams and 1.20 and 1.22 mm for the ^{44}S and ^{43}P beams. The statistical uncertainties in each of these results, corresponding to the minimum figure of merit $+1$, are on the order of 10^{-3} mm. We attribute the discrepancies between the best-fit simulations and the measured spectra, as well as the larger $\approx$0.1 mm observed variation among the best-fit bulge thicknesses, to variations in the momentum distributions of the incoming beams during the experiment and differences in the transverse positions of the two secondary beams on the (curved) target, leading to different effective target thicknesses. To determine the areal density of the target for use in cross-section calculations, we assume a bulge thickness of 1.09(13) mm, encompassing the full range of these results, yielding an areal density of 240(2) mg/cm^2. The midtarget beam energies and average beam velocities given in Table I were also determined using these simulations.

III. ANALYSIS AND RESULTS

Projectile-frame γ-ray spectra measured via inverse-kinematics proton scattering from ^{42,44}S and ^{41,43}P appear in Figs. 2–5. The average projectile velocities in Table I were used in the Doppler reconstruction of the γ rays emitted in flight. The solid curves in the figures are fits consisting of a linear combination of GEANT4 simulations of the response of GRETINA to the observed γ rays with a prompt background, shaded in gray, consisting of two exponential functions. The contribution of the nonprompt room background to the fits was negligible. The γ-ray energies and intensities extracted from the fits are listed in Table II. The γ-ray energies reported to the right in Table II were determined by varying the simulated energies of the emitted γ rays to optimize the fits of the response functions to the measured spectra. The error ranges correspond to 95% confidence intervals.

The position of the liquid hydrogen target relative to the focus of GRETINA along the beam axis strongly impacts the energies of γ rays in Doppler reconstruction. We found the target offset to be 11.1(4) mm by fixing the energy of the

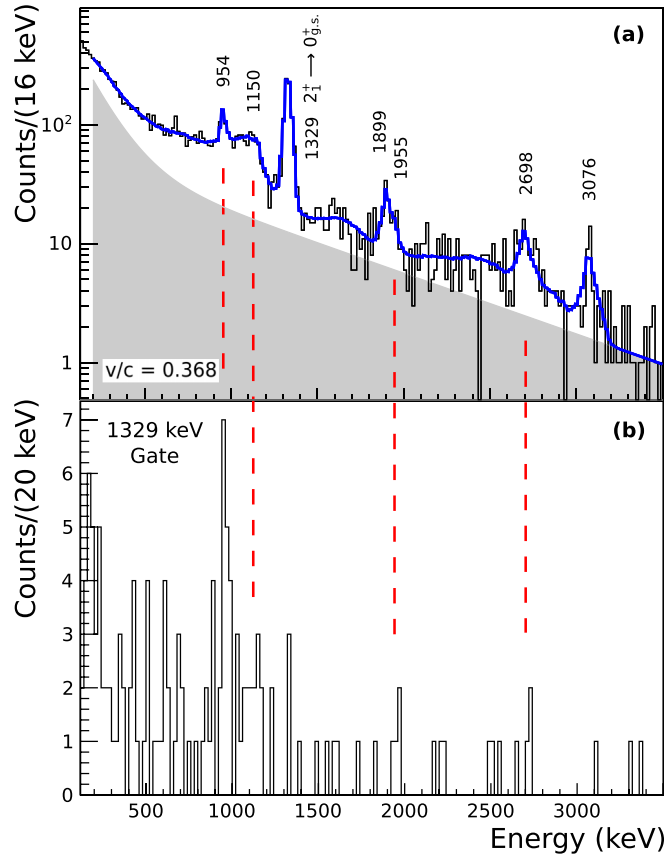

FIG. 3. (a) Projectile-frame spectrum of ^{44}S measured via inverse-kinematics proton scattering. (b) Proton-scattering spectrum gated on the 1329-keV γ ray.

1329-keV $2_1^+ \rightarrow 0^+_{gs}$ transition in ^{44}S and varying the target offset in simulations to obtain a best fit to the measured spectrum. We chose this transition because its energy was determined to a precision of 1 keV in a measurement of ^{44}S nuclei at rest in the laboratory [17]. The best fit to the 1329-keV peak along with a plot of the figure of merit from the log-likelihood fit vs the offset of the target along the beam axis appears in Fig. 6. We accounted for the mean lifetime of the 2_1^+ state of ^{44}S, deduced from the $B(E2; 0^+_{gs} \rightarrow 2^+)$ value measured via Coulomb excitation [18], of 3.5(10) ps in the simulations. However, we found that the impact of the lifetime on the resulting best-fit target offset was below 0.1 mm, a statistically insignificant effect relative to the 0.4-mm uncertainty in the result.

The mean lifetimes of the 2_1^+ state of ^{42}S of 20.6(15) ps and the 4^+ state of ^{44}S at 2457 keV of 76(24) ps reported by Parker *et al.* [3] are long enough to impact the Doppler-corrected γ-ray line shapes and were included in the simulations of the 903- and 1150-keV γ rays deexciting these states. These transitions were not observed with sufficient statistics in the present work to perform independent mean lifetime measurements. The line shapes corresponding to the γ rays deexciting the 173- and 188-keV first-excited states of ^{41}P and ^{43}P show low-energy tails consistent with lifetimes on the order tens to hundreds of picoseconds. The low-energy

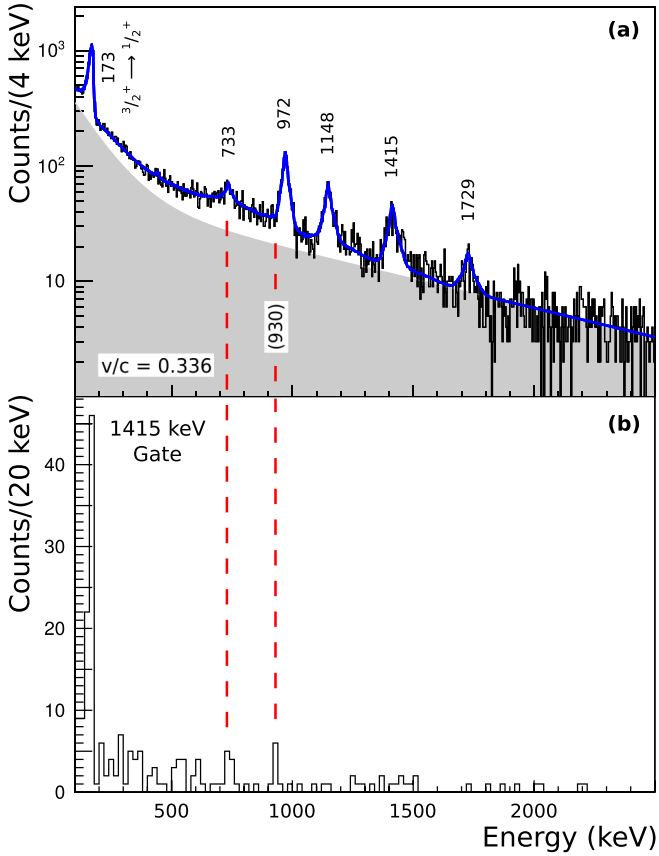

FIG. 4. (a) Projectile-frame spectrum of ^{41}P measured via inverse-kinematics proton scattering. (b) Proton-scattering spectrum gated on the 1416-keV γ ray.

regions of the projectile-frame γ-ray spectra of ^{41}P and ^{43}P are shown in Figs. 7 and 8. We varied both the energies and the mean lifetimes of the states to determine best-fit values of $\tau_{(3/2^+)} = 264(33)$ ps in ^{41}P and $\tau_{3/2^+} = 62(18)$ ps in ^{43}P. In both cases, the best-fit transition energy varies by less than 1 keV over the full uncertainty range of the mean lifetimes.

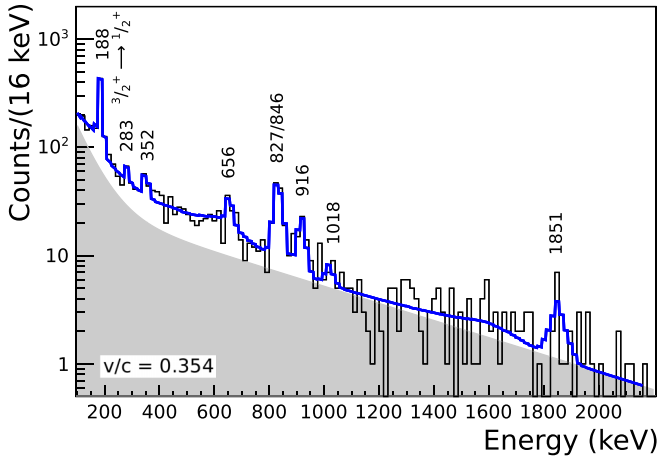

FIG. 5. Projectile-frame spectrum of ^{43}P measured via inverse-kinematics proton scattering.

TABLE II. Level energies, spins and parities, and γ-ray energies from Refs. [2,14–16] and γ-ray energies, relative intensities, and cross sections from the present work.

	E_{level} (keV)	J^π ($\hbar$)	E_γ (keV)	E_γ (keV)	I_γ (%)	σ (mb)
^{42}S		Ref. [14]				
	902	2^+	902(4)	903(2)	100(9)	23(6)
	2722	(4^+)	1820(4)	1820(30)	8(4)	2.4(12)
	3002	(2^+)	3002(4)	2990(30)	20(5)	6.2(15)
			2100(4)		<1	
			–	1570(30)	9(4)	
			–	2190(30)	8(4)	
^{44}S		Ref. [2]				
	1329	2^+	1329.0(5)	1329	100(4)	15(3)
	2283(4)	(2^+)	949(5)	954(4)	17(3)	4.5(8)
	2479(11)	(4^+)	1128(6)	1150(11)	11(3)	2.7(8)
	3264(6)	(2^+)	1891(10)	1899(6)	13(2)	3.7(7)
			1929(7)	1955(25)	2(2)	
	4027(13)		–	2698(13)	8(2)	2.1(5)
			–	3076(10)	8(2)	
^{41}P		Ref. [15]				
	173(1)	$(3/2^+)$	172(12)	173(1)	100(2)	6(2)
	1150(3)		964(22)	972(1)	43(2)	13.5(6)
			1146(28)	1148(2)	24(2)	
	1589(4)		1408(19)	1415(3)	23(2)	4.6(4)
			420(22)		<2	
	2324(6)		–	733(5)	6(1)	1.1(3)
			–	1729(5)	9(1)	
^{43}P		Ref. [16]				
	188(1)	$3/2^+$	184(1)	188(1)	100(6)	4(2)
	845(6)	$(5/2^+)$	845(4)	846(11)	15(7)	4.9(14)
			661(4)	656(6)	15(5)	
	1015(4)	$(5/2^+)$	825(5)	827(4)	38(8)	6.2(12)
	1104(5)	$(5/2^+)$	911(6)	916(5)	22(5)	3.5(8)
	2039	$(5/2^+)$	1851(11)	1851	7(4)	1.8(8)
			1018(6)		<8	
			–	283(6)	7(3)	
			–	352(13)	11(4)	

Plots of the figure of merit from the log-likelihood fits vs mean lifetime appear in the insets in Figs. 7 and 8. In addition to the statistical uncertainties, we have included the contribution of the 0.4-mm uncertainty in the position of the target along the beam axis in the error ranges. This is an 11% effect in ^{41}P and a 20% effect in ^{43}P.

Partial level schemes of ^{42,44}S and ^{41,43}P including the levels populated in the present work are shown in Fig. 9. We observe several known γ rays and have identified two new transitions in ^{42}S at 1570 and 2190 keV, which we are unable to place in the level scheme. In ^{44}S, we observe two new γ rays at 2696 and 3076 keV. We place the 2696-keV transition feeding the 2_1^+ state due to the fact that it is seen in the spectrum of γ rays measured in coincidence with the 1329-keV $2_1^+ \rightarrow 0_{\text{gs}}^+$ transition shown in Fig. 3(b). We are unable to place the 3076-keV transition in the level scheme. In ^{41}P, we place a new 733-keV transition in the level scheme on

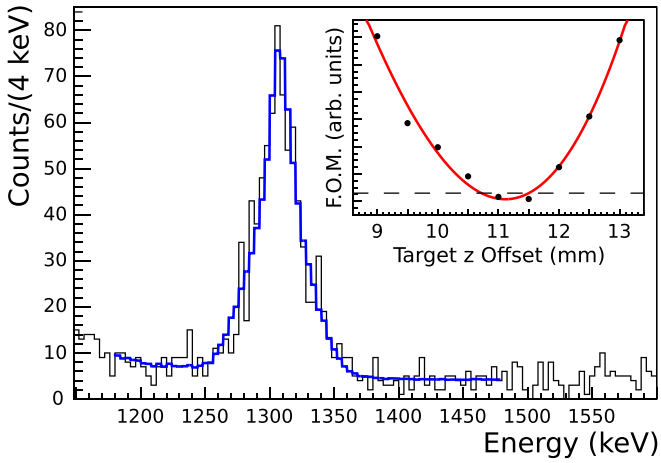

FIG. 6. The region of the projectile-frame spectrum of ^{44}S surrounding the photopeak of the 1329-keV γ ray deexciting the 2_1^+ state. The smooth curve is the GEANT4 fit corresponding to the best-fit value of the target offset from the focus of GRETINA along the beam axis of 11.1 mm. The inset shows the figure of merit from the fit vs the simulated target offset. The dashed line corresponds to the 95% confidence interval of 0.4 mm.

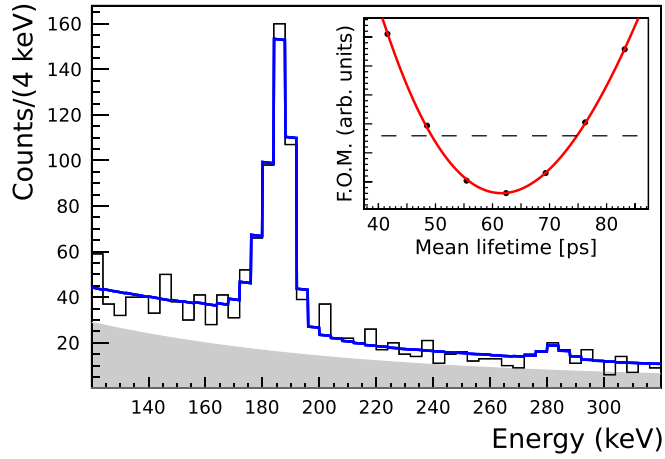

FIG. 8. The low-energy region of the projectile-frame spectrum of ^{43}P measured via inverse-kinematics proton scattering. The smooth curve is the GEANT4 fit corresponding to a mean lifetime of the $J^\pi = 3/2^+$ first-excited state of 62 ps. The inset shows the figure of merit from the fit vs. the simulated mean lifetime. The dashed line corresponds to the 95% confidence interval of ±12 ps.

the basis of its observation in coincidence with the 1415-keV gated spectrum in Fig. 4(b), where we also see a possible weak γ ray at ≈930 keV, which we are unable to confirm or place in the level scheme. The 420-keV transition observed by Bastin *et al.* [15] to deexcite the state at 1588 keV along with the 1415-keV γ ray, and which appears in Fig. 9 as a dashed arrow, was below our detection threshold. We are also unable to place a new 1729-keV transition. In ^{43}P, we included in the fit the 1018- and 1851-keV transitions deexciting the excited state at 2035 keV observed in one-proton knockout from ^{44}S [16]. We are only able to place an upper limit on the intensity of the 1018-keV transition. We are unable to place new 283- and 352-keV transitions.

The cross sections for inelastic proton scattering to excited states of ^{42,44}S and ^{41,43}P listed in Table II were determined from the measured γ-ray yields, corrected for feeding by transitions from higher-lying states, based on the partial level schemes in Fig. 9. In the case of the 2_1^+ state of ^{42}S, the 2100-keV γ ray observed to deexcite the 3002-keV (2^+) state by Lunderberg *et al.* [14] and shown as a dashed arrow in Fig. 9 was below our detection threshold. We included the 2100-keV γ ray in the fit to place an upper limit on its intensity, and we included that upper limit in the feeding correction. We observed γ rays, at 1570 and 2190 keV in ^{42}S and at 3076 keV in ^{44}S, that we could not place in the respective level schemes. We have included possible feeding of the 2_1^+ states by these

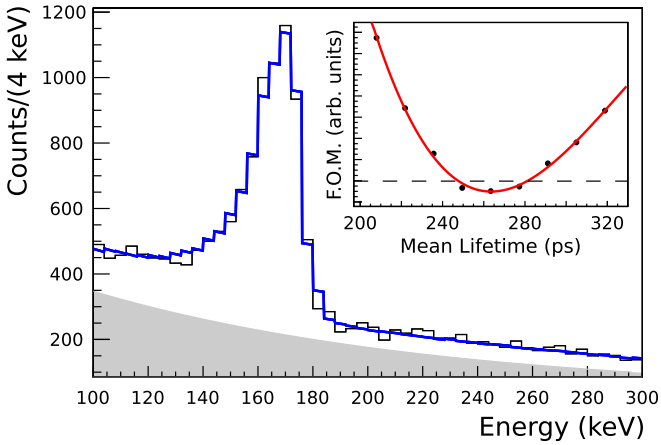

FIG. 7. The low-energy region of the projectile-frame spectrum of ^{41}P measured via inverse-kinematics proton scattering. The smooth curve is the GEANT4 fit corresponding to a mean lifetime of the $J^\pi = (3/2^+)$ first-excited state of 264 ps. The inset shows the figure of merit from the fit vs the simulated mean lifetime. The dashed line corresponds to the 95% confidence interval of 18 ps.

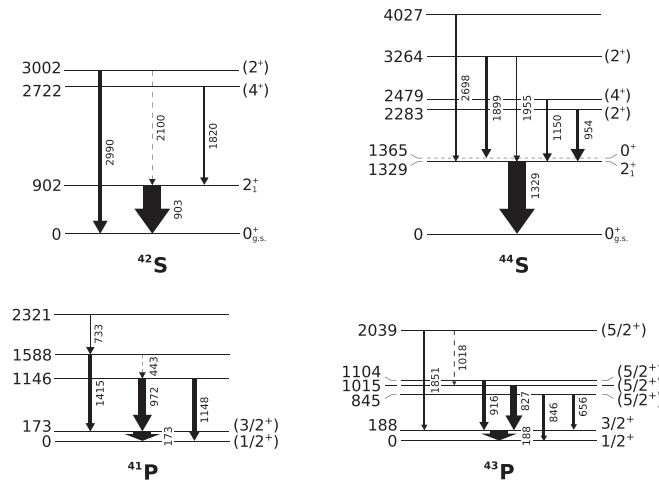

FIG. 9. Partial level schemes of ^{42,44}S and ^{41,43}P showing levels populated in the present work. Arrow widths are proportional to the measured γ-ray intensities.

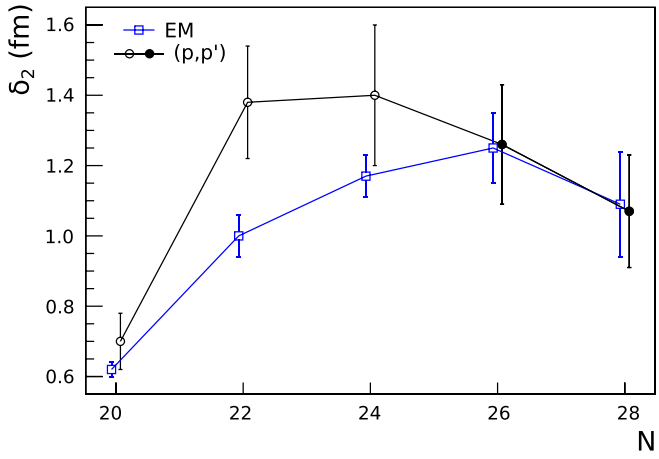

FIG. 10. Proton-scattering and electromagnetic deformation lengths δ_2 for the $0^+_{gs} \rightarrow 2^+_1$ excitations of even-even neutron-rich sulfur isotopes. Proton-scattering deformation lengths are from Ref. [22] (open circles) and the present work (solid circles), and electromagnetic deformation lengths (open squares) are from Ref. [23].

γ rays in the error ranges of the measured cross sections. We find cross sections for populating the 2^+_1 excitations via proton scattering of 23(6) mb in ^{42}S and 15(3) mb in ^{44}S.

We used the coupled-channels code ECIS97 [19] and the global optical potentials of Refs. [20] and [21] to determine deformation lengths from our measured cross sections for inelastic scattering to the 2^+_1 states of $\delta_2 = 1.26(17)$ fm for ^{42}S and 1.07(16) fm for ^{44}S. The error ranges include both the uncertainties in measured cross sections and any discrepancy due to the two global optical potential sets and the use of vibrational and rotational models. The impact of the choice of optical potential parameter set was 2% for ^{42}S and 7% in the case of ^{44}S. The variation in the deformation lengths determined using the vibrational and rotational models for the excitations was at the 3% level. Proton-scattering deformation lengths of the 2^+ states of even-even neutron-rich sulfur isotopes from the present work and Ref. [22] are plotted along with electromagnetic deformation lengths from the evaluation of Ref. [23] in Fig. 10.

We did not collect sufficient statistics to perform γ-ray angular distribution measurements. However, significant alignment of the residual nucleus can be expected in direct reactions with fast beams [24–26]. We used the ECIS calculations described above to evaluate the potential impact of γ-ray angular distributions on our measured γ-ray yields. We integrated the angular distributions from ECIS of the components t_{20} and t_{40} of the polarization tensor of the ^{42,44}S nuclei after excitation to their 2^+_1 states via (p, p') to determine their expectation values, which correspond to the orientation parameters B_2 and B_4 in the usual notation. We found roughly 30% oblate alignment for ^{42}S and 20% oblate alignment for ^{44}S, with very similar γ-ray angular distributions predicted by the vibrational and rotational models. Following the formalism outlined in Refs. [24,25], we calculated the corresponding angular distribution coefficients and performed simulations including the resulting γ-ray angular distributions and compared the resulting γ-ray yields with those obtained assuming isotropic γ-ray emission in the projectile frame. The predicted angular distribution affected the yield of the 903-keV γ ray in ^{42}S at the 3% level and that of the 1329-keV γ ray in ^{44}S at the 1% level. These effects fall well within the statistical uncertainties in the γ-ray yields. It is important to note that the significant feeding of the 2^+_1 states by deexcitations of higher-lying states leads to a reduced degree of alignment relative to these estimates.

IV. DISCUSSION

Given the importance of ^{42}Si and neighboring isotopes for building our understanding of nuclear structure close to the neutron drip line, a range of observables in these nuclei should be measured and understood. In this section, we use the present ^{42,44}S(p, p') results to extract M_n/M_p, the ratio of the neutron and proton transition matrix elements for the $0^+_{gs} \rightarrow 2^+_1$ excitations, which provides insights about the presence or absence of closed shells. In addition, we use the ^{41,43}P(p, p') results to add to a comparison of the SDPF-U and SDPF-MU shell-model interactions recently begun by Gade *et al.* [6] in a study of ^{42}Si.

The comparison of the present ^{42,44}S(p, p') results on the $0^+_{gs} \rightarrow 2^+_1$ excitations with the previous Coulomb excitation measurements of the same transitions [18,27] allows us to determine M_n/M_p. Coulomb excitation measures the proton transition matrix element exclusively, while proton scattering involves both the proton and the neutron transition matrix elements. If the excitation is isoscalar, then the ratio M_n/M_p of the neutron and proton transition matrix elements is equal to the ratio N/Z of the neutron and proton numbers, and hence $(M_n/M_p)/(N/Z)$ is equal to 1. This ratio is determined from the proton inelastic-scattering deformation length $\delta_{(p,p')}$ and the proton deformation length δ_p using the equation [28]

$$\frac{M_n}{M_p} = \frac{b_p}{b_n}\left[\frac{\delta_{(p,p')}}{\delta_p}\left(1 + \frac{b_n}{b_p}\frac{N}{Z}\right) - 1\right], \quad (1)$$

where b_n/b_p is the ratio of the sensitivities of the proton-scattering reaction to the neutron and proton contributions to the excitation. The ratio b_n/b_p is approximately 3 at proton energies below 50 MeV and approximately 1 at 1 GeV. However, there is considerable uncertainty about the value of b_n/b_p at the energy of this experiment: 60–70 MeV in the center of mass frame. So for the purposes of the present analysis, we assume that $b_n/b_p = 2 \pm 1$, which despite the large uncertainty allows us to reach important conclusions about the present measurements.

Figure 11 illustrates the values of $(M_n/M_p)/(N/Z)$ for the $0^+_{gs} \rightarrow 2^+_1$ excitations in the $N = 20$–30 even-even isotopes of Si, S, Ar, and Ca. We have combined proton-scattering deformation lengths from the present work and Refs. [22,29–33] with the proton deformation lengths of Ref. [23]. Of the isotopes shown in the plot, only two vary substantially from the value of $(M_n/M_p)/(N/Z) = 1$ expected for isoscalar transitions—the $N = 28$ and 30 isotopes of Ca, which have a closed major proton shell ($Z = 20$). The $(M_n/M_p)/(N/Z)$ values for these two isotopes reflect the fact that, while there are valence neutrons to contribute to the $0^+_{gs} \rightarrow 2^+_1$ excitation,

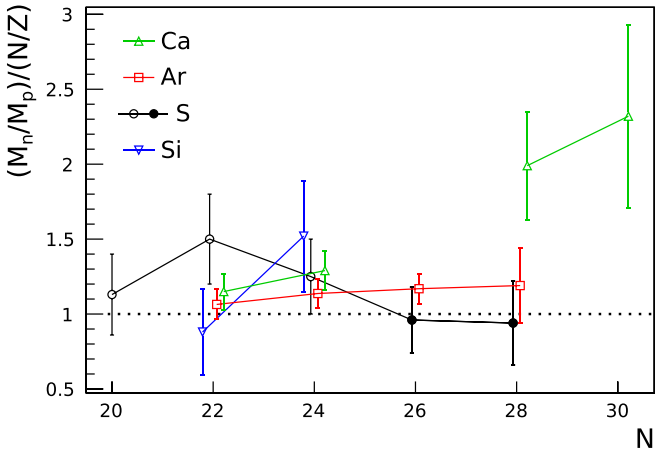

FIG. 11. Ratios of neutron to proton transition matrix elements M_n/M_p expressed relative to N/Z for even-even neutron-rich calcium, argon, sulfur, and silicon isotopes from Refs. [22,29–33] (open symbols) and the present work (solid circles).

there are no valence protons. Therefore, the only proton contributions must result from the mechanism of core polarization. The results from the present work, $(M_n/M_p)/(N/Z) = 0.96(22)$ for ^{42}S and $(M_n/M_p)/(N/Z) = 0.94(28)$ for ^{44}S, are both statistically consistent with 1.0.

In Fig. 12, the measured values for the $N = 28$ isotones are compared with shell-model calculations performed with the SDPF-U [34] and SDPF-MU [35] effective interactions. For both sets of shell -model calculations, M_p and M_n are calculated using the "bare" transition matrix elements A_p and A_n and a parameter d that reflects core polarization in the transitions:

$$M_p = A_p(1+d) + A_n(d),$$
$$M_n = A_p(d) + A_n(1+d). \quad (2)$$

We adopt $d = 0.5$, which gives effective charges of $e_p = 1.5$ and $e_n = 0.5$ for the electromagnetic transitions, values that were used in Ref. [6].

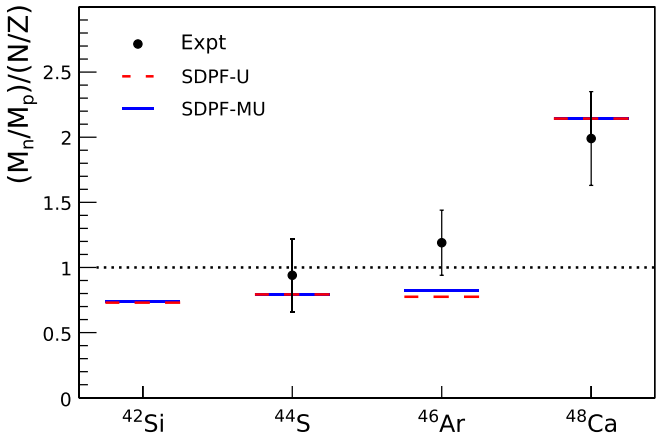

FIG. 12. Ratios of neutron to proton transition matrix elements M_n/M_p expressed relative to N/Z for even-even $N = 28$ isotones from Ref. [30] and the present work compared with shell-model predictions, described in the text.

Calculations with both the SDPF-U and SDPF-MU interactions give identical or very similar M_n/M_p values, with the largest discrepancy of 6% for ^{46}Ar. The calculations predict that for ^{42}Si, ^{44}S, and ^{46}Ar $M_n/M_p < N/Z$, signaling that protons play a disproportionately large role in the $0^+_{gs} \rightarrow 2^+_1$ excitations. The present ^{44}S(p, p') data are not sufficient to distinguish between the isoscalar situation $(M_n/M_p = N/Z)$ and the shell-model predictions of $M_n/M_p = 0.7$.

The shell-model predictions for Mn/Mp in ^{42}Si, ^{44}S, and ^{46}Ar are provocative. An M_n/M_p value of less than N/Z generally indicates a closed neutron shell. Given the collapse of the $N = 28$ shell closure in ^{42}Si and ^{44}S, the shell-model predictions for M_n/M_p in those nuclei are interesting and important to test experimentally.

To determine whether the M_n/M_p values for ^{42}Si, ^{44}S, and ^{46}Ar are less than N/Z and consistent with the shell-model predictions with statistical confidence, three issues will have to be addressed. First, the uncertainty in the (p, p') data for these nuclei will have to be reduced by increasing the numbers of counts in the experimental spectra significantly—and; the new Facility for Rare Isotope Beams (FRIB) will have that capability. Second, a precise Coulomb excitation measurement of ^{42}Si is needed, and the uncertainty in the Coulomb excitation result for ^{44}S will need to be improved, once again through the improvement in statistics possible at FRIB.

Third, we must address the uncertainty in the ratio b_n/b_p, for which we have used the value 2 ± 1. Remarkably, this issue will be addressed at FRIB as well. The beams in the present work were at energies of 70 MeV/nucleon and lower, energies for which there is considerable uncertainty regarding the value of b_n/b_p for inverse kinematics (p, p') reactions. At FRIB, intense beams ($>10^4$ particles per second) of ^{42}Si, ^{44}S, and ^{46}Ar will be available at energies much greater than 100 MeV/nucleon. It has been known for more than 30 years that inelastic hadron scattering at energies over 100 MeV is approximately isoscalar; that is, it has $b_n/b_p \approx 1$ (for example, see Ref. [36]). Therefore, performing inverse kinematics (p, p') reactions at FRIB will nearly eliminate the uncertainty in the value of b_n/b_p.

The present ^{41,43}P(p, p') results provide an opportunity to expand upon the recently reported comparison of the SDPF-U [34] and SDPF-MU [35] shell-model interactions using a measurement of the level scheme of ^{42}Si via the one-proton knockout reaction [6]. The authors of Ref. [6] demonstrated that the SDPF-U interaction predicted a number of states at low excitation energy (below 4 MeV) that was significantly larger than what was observed in the experiment. In contrast, SDPF-MU predicted a smaller number of states in the same range of excitation energy that more accurately reflected the observed spectrum. The authors of the ^{42}Si study therefore concluded that SDPF-MU is a more useful interaction for investigating the effects of weak binding in ^{40}Mg. Here, we find that SDPF-MU is also better able to describe the more deeply bound P isotopes in the neighborhood of ^{42}Si.

In Fig. 13, we compare the cross sections of the states observed here in ^{41}P(p, p') with the distribution of (p, p') strength, $B(p, p')$, predicted using the SPDF-U and SPDF-MU interactions. The strength $B(p, p')$ is calculated for each state

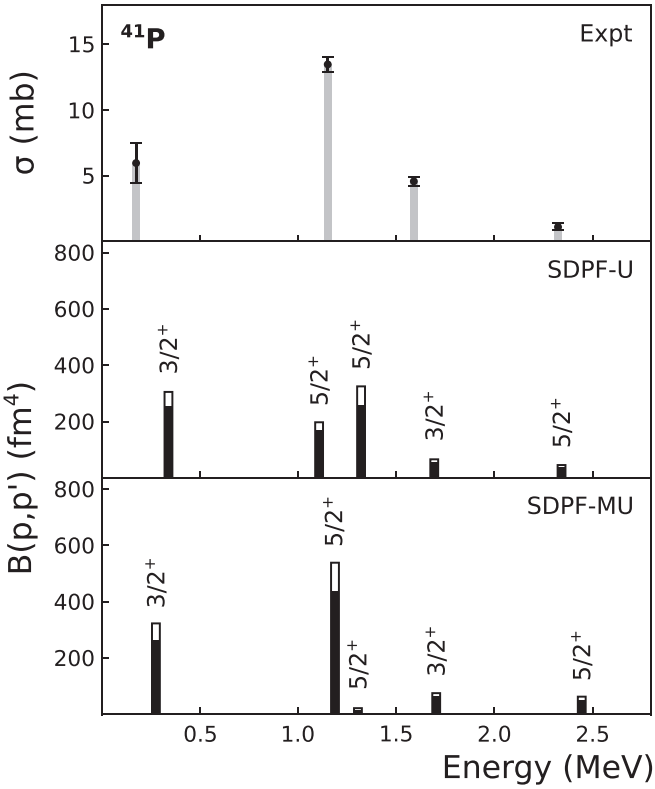

FIG. 13. Measured cross sections for populating excited states in ^{41}P (top panel) compared with shell-model predictions of the proton-scattering transition strength $B(p, p')$ calculated using the SPDF-U [34] (middle panel) and SPDF-MU [35] (bottom panel) effective interactions. In the bottom panels, the solid bars correspond to $b_n/b_p = 1$ and the open bars to $b_n/b_p = 3$.

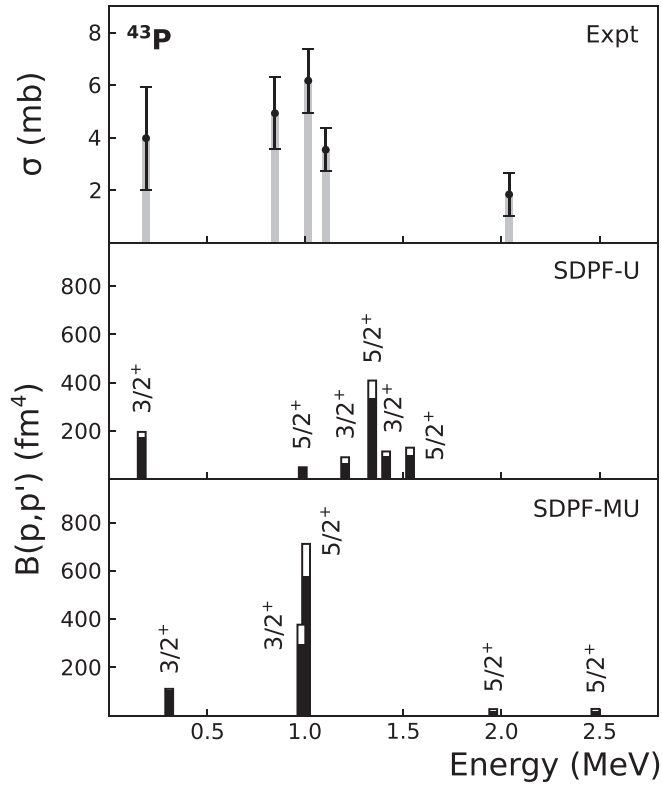

FIG. 14. Measured cross sections for populating excited states in ^{43}P (top panel) compared with shell-model predictions of the proton-scattering transition strength $B(p, p')$ calculated using the SPDF-U [34] (middle panel) and SPDF-MU [35] (bottom panel) effective interactions. In the bottom panels, the solid bars correspond to $b_n/b_p = 1$ and the open bars to $b_n/b_p = 3$.

using the proton (M_p) and neutron (M_n) transition matrix elements for the decay from the state to the ground state using the following equation:

$$B(p, p') = \frac{1}{(2J_i + 1)}(C_p M_p + C_n M_n)^2, \quad (3)$$

where $J_i = 1/2$, because the ground states of both ^{41,43}P have $J = 1/2$. M_n and M_p are calculated for ^{41,43}P in the same way that the corresponding values are calculated for the even-even isotopes (as described in the discussion above). The normalized coefficients C_p and C_n account for the sensitivity of (p, p') to protons and neutrons and take on the values $C_p = C_n = 0.5$ for $b_n/b_p = 1$ and $C_p = 0.25$ and $C_n = 0.75$ for $b_n/b_p = 3$. In the bottom two panels of Fig. 13 the solid bars correspond to $b_n/b_p = 1$, and the open bars correspond to $b_n/b_p = 3$. The values between the top of the solid bar and the top of the open bar correspond to the range $b_n/b_p = 2 \pm 1$.

Figure 13 shows that both the SDPF-U and SDPF-MU interactions reproduce the experimental observation of the strong excitation of the first-excited state in ^{41}P, which has $J^\pi = 3/2^+$. SDPF-U gives two strong $5/2^+$ states at about 1.1 MeV, while SDPF-MU gives only one. The experiment shows only one strong state at that energy, so that observation favors the SDPF-MU interaction. The experiment shows a state near 1.6 MeV and another near 2.4 MeV. Both SDPF-U and SDPF-MU give such states—with a $3/2^+$ state near 1.6 MeV and a $5/2^+$ state near 2.4 MeV. We conclude that the comparison of the theoretical calculations with the data on ^{41}P favors SDPF-MU.

Figure 14 illustrates the situation in ^{43}P. As in ^{41}P, the experiment shows that the lowest excited state is strongly excited and that excitation is reproduced by both the SDPF-U and the SDPF-MU interactions. In the experiment, there is a cluster of three strongly populated states near 1 MeV. While SDPF-MU predicts two strongly populated states near 1 MeV (one having $J^\pi = 3/2^+$ and the other $J^\pi = 5/2^+$), the SDPF-U interaction gives a cluster of five states distributed from 1.0 to 1.5 MeV, with the strongest being a $5/2^+$ state near 1.4 MeV. We conclude that the SDPF-MU interaction gives a better accounting of the situation in ^{43}P than SDPF-U does. In short, the present results on ^{41,43}P(p, p') and the recently reported ^{42}Si results all favor the SDPF-MU interaction in this neutron-rich region.

V. CONCLUSIONS

Comparison of the proton inelastic scattering measurement of the $0^+_{gs} \rightarrow 2^+_1$ excitation in ^{44}S reported here with previous Coulomb excitation measurements of the same excitation gives an M_n/M_p value that is, because of experimental

uncertainties, consistent with both the isoscalar value of N/Z and the shell-model prediction that $M_n/M_p = 0.7(N/Z)$, which would indicate that proton excitations play a disproportionately large role in this excitation and that there is a residual $N = 28$ shell closure effect. However, the higher beam rates and the higher beam energies available at FRIB will provide an opportunity to resolve this issue not only in ^{44}S but also in ^{42}Si. The ^{41,43}P(p, p') measurements reported here provide a means for expanding upon the comparison of the SDPF-U and SDPF-MU shell-model interactions begun in a recent study of ^{42}Si [6]. As in the case of ^{42}Si, the present results favor the SDPF-MU interaction.

ACKNOWLEDGMENTS

This work was supported by the National Science Foundation under Grants No. PHY-1617250, No. PHY-1064819, No. PHY-1565546, and No. 1401574 and by the U.S. Department of Energy under Grant No. DE-SC0009883. GRETINA was funded by the DOE, Office of Science. Operation of the array at the NSCL was supported by the DOE under Grants No. DE-SC0014537 (NSCL) and No. DE-AC02-05CH11231 (LBNL). We also thank T. J. Carroll for the use of the Ursinus College Parallel Computing Cluster, supported by the NSF under Grant No. PHY-1607335.

[1] T. Burrows, Nucl. Data Sheets **107**, 1747 (2006).
[2] J. Chen, B. Singh, and J. A. Cameron, Nucl. Data Sheets **112**, 2357 (2011).
[3] J. J. Parker *et al.*, Phys. Rev. Lett. **118**, 052501 (2017).
[4] J. Chen and B. Singh, Nucl. Data Sheets **135**, 1 (2016).
[5] J. Chen, Nucl. Data Sheets **140**, 1 (2017).
[6] A. Gade, B. A. Brown, J. A. Tostevin, D. Bazin, P. C. Bender, C. M. Campbell, H. L. Crawford, B. Elman, K. W. Kemper, B. Longfellow, E. Lunderberg, D. Rhodes, and D. Weisshaar, Phys. Rev. Lett. **122**, 222501 (2019).
[7] A. Gade and B. M. Sherrill, Phys. Scr. **91**, 053003 (2016).
[8] D. J. Morrissey, B. M. Sherrill, M. Steiner, A. Stolz, and I. Wiedenhöver, Nucl. Instrum. Methods Phys. Res., Sect. B **204**, 90 (2003).
[9] D. Bazin, J. A. Caggiano, B. M. Sherrill, J. Yurkon, and A. Zeller, Nucl. Instrum. Methods Phys. Res., Sect. B **204**, 629 (2003).
[10] H. Ryuto, M. Kunibu, T. Minemura, T. Motobayashi, K. Sagara, S. Shimoura, M. Tamaki, Y. Yanagisawa, and Y. Yano, Nucl. Instrum. Methods Phys. Res., Sect. A **555**, 1 (2005).
[11] S. Paschalis *et al.*, Nucl. Instrum. Methods Phys. Res., Sect A **709**, 44 (2013).
[12] D. Weisshaar *et al.*, Nucl. Instrum. Methods Phys. Res., Sect. A **847**, 187 (2017).
[13] S. Agostinelli *et al.* (geant4 Collaboration), Nucl. Instrum. Methods Phys. Res., Sect. A **506**, 250 (2003).
[14] E. Lunderberg, A. Gade, V. Bader, T. Baugher, D. Bazin, J. S. Berryman, B. A. Brown, D. J. Hartley, F. Recchia, S. R. Stroberg, D. Weisshaar, and K. Wimmer, Phys. Rev. C **94**, 064327 (2016).
[15] B. Bastin *et al.*, Phys. Rev. Lett. **99**, 022503 (2007).
[16] L. A. Riley, P. Adrich, T. R. Baugher, D. Bazin, B. A. Brown, J. M. Cook, P. D. Cottle, C. A. Diget, A. Gade, D. A. Garland, T. Glasmacher, K. E. Hosier, K. W. Kemper, T. Otsuka, W. D. M. Rae, A. Ratkiewicz, K. P. Siwek, J. A. Tostevin, Y. Utsuno, and D. Weisshaar, Phys. Rev. C **78**, 011303(R) (2008).
[17] C. Force *et al.*, Phys. Rev. Lett. **105**, 102501 (2010).
[18] T. Glasmacher, B. A. Brown, M. J. Chromik, P. D. Cottle, M. Fauerbach, R. W. Ibbotson, K. W. Kemper, D. J. Morrissey, H. Scheit, D. W. Sklenicka, and M. Steiner, Phys. Lett. B **395**, 163 (1997).
[19] J. Raynal, Phys. Rev. C **23**, 2571 (1981); "ECIS97" (unpublished).
[20] A. J. Koning and J.-P. Delaroche, Nucl. Phys. A **713**, 231 (2003).
[21] F. D. Becchetti and G. W. Greenlees, Phys. Rev. **182**, 1190 (1969).
[22] F. Maréchal *et al.*, Phys. Rev. C **60**, 034615 (1999).
[23] B. Pritychenko, M. Birch, M. Horoi, and B. Singh, Nucl. Data Sheets **120**, 112 (2014).
[24] H. Olliver, T. Glasmacher, and A. E. Stuchbery, Phys. Rev. C **68**, 044312 (2003).
[25] A. E. Stuchbery, Nucl. Phys. A **723**, 69 (2003).
[26] S. Takeuchi, T. Motobayashi, Y. Togano, M. Matsushita, N. Aoi, K. Demichi, H. Hasegawa, and H. Murakami, Nucl. Instrum. Methods Phys. Res., Sect. A **763**, 596 (2014).
[27] H. Scheit, T. Glasmacher, B. A. Brown, J. A. Brown, P. D. Cottle, P. G. Hansen, R. Harkewicz, M. Hellström, R. W. Ibbotson, J. K. Jewell, K. W. Kemper, D. J. Morrissey, M. Steiner, P. Thirolf, and M. Thoennessen, Phys. Rev. Lett. **77**, 3967 (1996).
[28] A. M. Bernstein, V. R. Brown, and V. A. Madsen, Phys. Lett. B **103**, 255 (1981).
[29] A. M. Bernstein, V. R. Brown, and V. A. Madsen, Comments Nucl. Part. Phys. **11**, 203 (1983).
[30] L. A. Riley, M. L. Agiorgousis, T. R. Baugher, D. Bazin, M. Bowry, P. D. Cottle, F. G. DeVone, A. Gade, M. T. Glowacki, K. W. Kemper, E. Lunderberg, D. M. McPherson, S. Noji, F. Recchia, B. V. Sadler, M. Scott, D. Weisshaar, and R. G. T. Zegers, Phys. Rev. C **90**, 011305(R) (2014).
[31] H. Scheit, F. Maréchal, T. Glasmacher, E. Bauge, Y. Blumenfeld, J. P. Delaroche, M. Girod, R. W. Ibbotson, K. W. Kemper, J. Libert, B. Pritychenko, and T. Suomijärvi, Phys. Rev. C **63**, 014604 (2000).
[32] L. A. Riley *et al.*, Phys. Rev. C **72**, 024311 (2005).
[33] C. Campbell *et al.*, Phys. Lett. B **652**, 169 (2007).
[34] F. Nowacki and A. Poves, Phys. Rev. C **79**, 014310 (2009).
[35] Y. Utsuno, T. Otsuka, B. A. Brown, M. Honma, T. Mizusaki, and N. Shimizu, Phys. Rev. C **86**, 051301(R) (2012).
[36] J. J. Kelly, Phys. Rev. C **37**, 520 (1988).